INSTITUTE OF PHYSICS PUBLISHING JOURNAL OF MICROMECHANICS AND MICROENGINEERING

J. Micromech. Microeng. **11** (2001) 1–12 www.iop.org/Journals/jm PII: S0960-1317(01)19341-1

# Modeling and control of piezoelectric cantilever beam micro-mirror and micro-laser arrays to reduce image banding in electrophotographic processes

**Hung-Ming Cheng**[1], **Michael T S Ewe**[1], **Rashid Bashir**[2,3,4] **and George C T Chiu**[1]

[1] School of Mechanical Engineering, Purdue University, West Lafayette, Indiana 47907, USA
[2] School of Electrical and Computer Engineering, Purdue University, West Lafayette, Indiana 47907, USA
[3] Department of Biomedical Engineering, Purdue University, West Lafayette, Indiana 47907, USA

E-mail: bashir@ecn.purdue.edu

Received 24 November 2000



**Abstract**

This paper present a theoretical evaluation of the application of microelectromechanical technology to reduce banding artifacts in electrophotographic printing systems. The proposed system would consist of arrays of micro-mirrors and micro-lasers replacing conventional laser printing mechanisms. Several advantages of the new system include faster printing speeds, elimination of synchronization problems, improved image quality and lower production costs. Each micro-mirror can be a surface micro-machined piezoelectric cantilever beam with a reflective surface. An analytical model for the cantilever beam describing the dynamic relationship between scan line deflection and the applied voltage is derived. Using a closed-loop feedback control strategy, the effectiveness of the micro-mirror arrays in reducing banding was theoretically evaluated. Calculations show that each micro-mirror should be capable of deflecting the scan line a distance of 50 $\mu$m or approximately one 600 dots per inch (dpi) pixel by only using a 2 V voltage potential. Using an actual measured line spacing sequence, the operation of the system was simulated. The results demonstrated good tracking and significant reduction of the low-frequency banding components. Emulated images showed significant reduction in banding for a typical 600 dpi print resolution.

## 1. Introduction

The electrophotographic (EP) process is widely used in laser printers to generate high-quality images on paper. In conventional laser printers, a latent image is formed on an organic photoconductive (OPC) drum using a pulsed laser beam that is scanned across the OPC drum by a spinning polygon mirror, as shown in figure 1. Toner particles are then electrostatically 'developed' onto the latent image. The image is later transferred onto a sheet of paper as the paper comes in contact with the OPC drum. However, due to velocity variation of the OPC drum, a type of image artifact called *banding* will be present on the printouts. Banding is a type of artifact that appears as light and dark bands oriented across a printed page perpendicular to the process direction, as shown in figure 2. The defect is generated because of the non-uniformity of the OPC drum velocity and the failure to position the scan lines at the desired location due to the gear-to-gear errors. It is also attributed to vibrations within the printer caused by other engine components such as the cleaning blade. The wobbling of the spinning polygon mirror also causes high-frequency banding. Since reducing banding often requires

[4] Author to whom correspondence should be addressed.

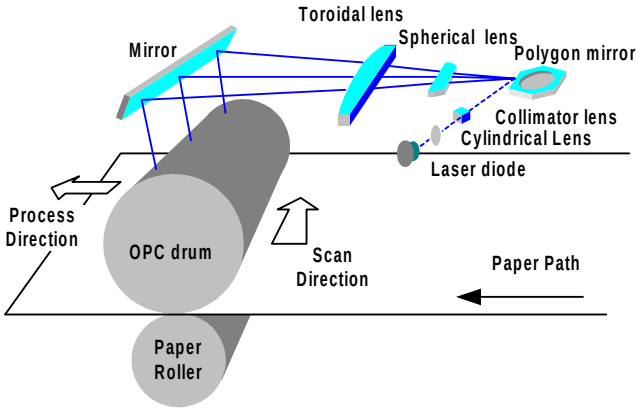


**Figure 1.** Basic arrangement of the optical components in a laser printer.

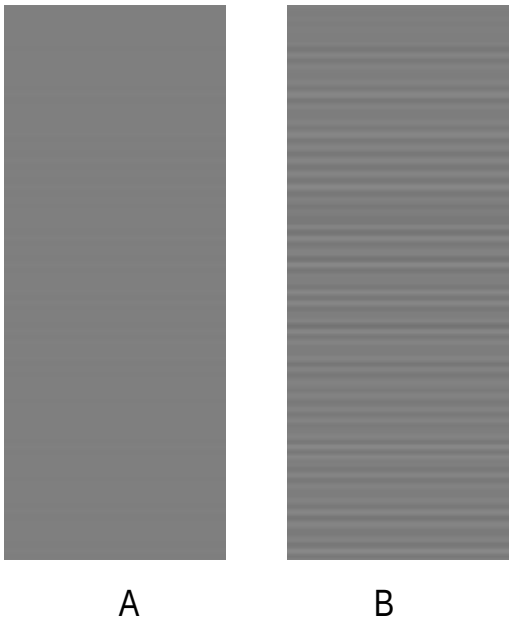


**Figure 2.** Comparison between a *A* normal printout and *B* a printout with banding. Both printouts are printed with 25% fill.

very small precise movements ($<5$ $\mu$m) of the laser beam, micro-technology is definitely a means to solve the problem.

Banding in EP processes has been well characterized by many researchers. The main sources of this print defect have been extensively studied and understood. Loce *et al* [1] modeled vibration-induced halftone banding in laser printers and pointed out that vibration within the EP print engine is mainly due to disturbances in the main drive mechanism of the EP process. Schubert [2] studied periodic image artifacts, which resulted from imperfect scanning hardware and the wobbling of the rotating polygon mirror. In Schubert's study, the human visual model is used to examine the visual sensitivity of banding. He also concluded that the line placement errors should be held to within 1% of the nominal value to successfully reduce banding at a particular frequency. Burns *et al* [3] pointed out that the laser beam positioning error would result in undesirable image noise, which degrades the image quality. Kawamoto *et al* [4, 5] verified that the contact charge roller and the cleaning blade both contribute to excited structural vibration and resulted in the OPC drum velocity variation. Melnychuck and Shaw [6] identified a strong correlation between the scan line spacing variation and the occurrence of banding.

Although banding is one of the most undesirable artifacts in EP printing, very few approaches have been documented in the literature that compensate for banding. Banding can be addressed mechanically by making more precise gears and mountings. Loce *et al* [7] proposed a method of using a multi-beam scanning system to compensate for banding by spacing the beams appropriately to suppress banding at certain frequencies. Later, other researchers proposed methods to reduce banding by deflecting the scanning laser beam using galvanometers or electric motors to compensate for the line spacing errors caused by the OPC drum velocity perturbation [8, 9]. Although these macro-scale implementations are feasible, they are often not cost effective in the competitive printer market. One advantage of using micro-technology is the ability to batch-fabricate the transducers, thus lowering the overall production cost.

Several researchers have successfully integrated micro-electromechanical (MEMS) devices with high-precision optical applications [10–13]. Commercial applications involving the use of micro-mirror arrays in digital light projection systems have also emerged over the past few years [14, 15]. Most of these micro-mirror devices use electrostatic actuation as the means to switch between the desired on or off states in a binary fashion. However, for the application described in this paper, a more continuous type of positioning system is required. Therefore an accurate and highly controllable micro-positioning actuation mechanism is required. Piezoelectric bending actuation is the most suitable choice because of its fast response, high bandwidth, high linearity and large force output. In addition, piezoelectric actuators generate no magnetic field in the conversion of electrical energy into mechanical motion.

The piezoelectric cantilever bending beam proposed in this paper consists of a flat strip of piezoelectric material and a strip of elastic material joined over the longitudinal surfaces. When an electric field is applied across the electrodes, the piezoelectric layer elongates while the elastic strip remains constant, creating a net bending motion. The motion of the tip can be considerable, making these devices useful tools as electromechanical actuators. Several researchers have developed models and formulated equations to characterize the behavior of piezoelectric cantilevers. Smits and Choi [16] developed the constituent equations for piezoelectric heterogeneous bimorphs subjected to various electrical and mechanical boundary conditions. The different mechanical boundary conditions considered in their work include a mechanical moment and a point force at the tip of the beam as well as a uniform load over the entire length of the bender. They used the internal energy approach assuming a thermodynamic equilibrium. Smits and Ballato [17] later derived a dynamic admittance matrix for piezoelectric cantilever bimorphs relating harmonically varying driving parameters to the response parameters. Low and Guo [18] modeled a three-layer piezoelectric bimorph beam with hysteresis. They fabricated a bimorph actuator and performed experiments to verify the model. Smits *et al* [19] later determined the resonance and antiresonance for both symmetric and asymmetric cantilevered piezoelectric flexors.

Several other researchers applied various control strategies to control piezoelectric actuators, including linear quadratic Gaussian control [20] and $H_\infty$ robust control [21].

In the past two decades, progress in micro-fabrication technology fueled the growth of the MEMS industry. Advantages of MEMS devices including higher bandwidth and lower power consumption increased its potential to replace traditional mechanical processes. Currently, the speed of the laser printing process is limited by the bandwidth of the mechanical components such as the spinning polygon mirror. By incorporating MEMS technology into the system, the spinning polygon mirror can be replaced by a cheaper and more robust micro-device, which can result in higher printing speeds.

This paper proposes and theoretically evaluates the application of MEMS technology to reduce the appearance of image banding in laser printing systems. The proposed system incorporating both micro-mirror and micro-laser arrays is first presented. An analytical model of the cantilever beam is then presented, followed by a summary of the proposed fabrication process. Using the formulated model, a closed-loop control strategy is employed to reduce the appearance of banding. Simulation results are then presented, using actual scan-line positioning errors from a typical laser printer. Simulated images are also presented to demonstrate the effectiveness of this technology in reducing banding. Conclusions and future research issues are presented in the last section.

## 2. Proposed system

The proposed system is designed to improve the printing speed and to reduce the artifacts that appear with conventional laser printing. Instead of using a polygon mirror and a single laser diode, the new approach uses arrays of micro-mirrors and micro-lasers, as shown in figure 3. Each of the individual micro-mirrors is a piezoelectric cantilever structure capable of deflecting the laser beam to adjust for scan line positioning errors in the process direction. Several advantages can be obtained by adopting this new system. First, the synchronization problem between the OPC drum velocity and the spinning polygon mirror can be removed. The unstable jittering commonly caused by the wobbling of the polygon mirror can also be eliminated. In addition, the printing process can proceed in a line-by-line fashion compared to the conventional raster order pixel-by-pixel printing, which will result in a higher printing speed. The printing speed will ultimately depend of the main drive mechanism. Using denser arrays can also dramatically increase the print resolution. Most important of all, the proposed system is capable of reducing banding artifacts in images.

### *2.1. Micro-mirror array*

Over the past decade, micro-mirror arrays have been integrated in MEMS applications. In 1999, Texas Instruments successfully fabricated 1.3 million tiny mirrors into a 4 $cm^2$ square panel with the bandwidth of each individual mirror as high as 50 kHz. The micro-mirror arrays were implemented in a digital micro-mirror display (DMD) used for a light projection system. However, the DMD is only suitable for digital applications, which requires only two discrete states (on or off). To reduce banding in EP processes, analog driven micro-mirrors are necessary to be able to adjust for the small displacements in a continuous fashion.

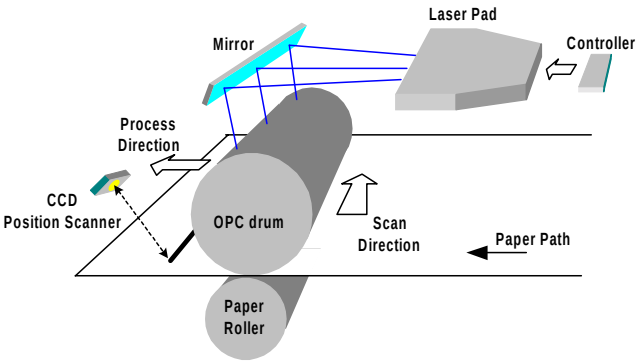


**Figure 3.** Proposed printing mechanism based on the proposed MEMS technology.

### *2.2. Micro-laser array*

The binary video signal corresponding to the halftone (1-bit) image data are projected onto the paper by rapidly pulsing an array of micro-lasers. Each laser in the array is individually addressable by a modulated image signal. Several issues that need to be taken into consideration include the power consumption, the laser firing bandwidth and thermal effects. The power consumption of the micro-lasers should be as low as possible for practical purposes. Hargis *et al* [15] investigated the power consumption of various applications of micro-lasers. Table 1 shows the possible power consumptions of several lasers. Near-infrared (near-IR) diode lasers, such as AlGaAs quantum well devices, are used to longitudinally pump the micro-lasers. The diode laser wavelength can be temperature-tuned to a strong absorption band of a rare earth ion, thus allowing very efficient operation. The Laser Power Co. fabricated micro-laser arrays capable of achieving a 1 MHz modulation bandwidth for individual elements, which meets both the criteria of low power consumption and high signal conversion bandwidth.

### *2.3. Printing mechanism*

Figure 4 shows the basic unit of the proposed printing mechanism. Each unit contains a set of micro-laser and micro-mirror arrays. The number of mirrors and lasers in the array is determined by the desired printing resolution. For an $N$ dots per inch (dpi) resolution printer, the device needs at least $8N$ pixels (8 inches across a page) to form a scan line. Assuming a print resolution of 600 dpi, a total of 4800 micro-mirrors are needed to generate a scan line. The micro-mirrors and micro-lasers are distributed into five separate arrays for ease of fabrication and packaging. Each of the five arrays contains 960 tiny mirrors and covers approximately one-fifth of a scan line. The dimensions of the micro-mirrors are specified for packaging purposes. The dimension for each single mirror used in the array is assumed to be 200 $\mu$m $\times$ 50 $\mu$m $\times$ 8.5 $\mu$m. Therefore, the dimensions of the die containing the 960 mirrors in an array are 2.4 mm $\times$ 4 mm (12 units $\times$ 80 units). For the

**Table 1.** Display type (note CRT denotes cathode-ray tube), efficiency and cost of micro-lasers.

| Display | Efficiency (Lumens $W^{-1}$) | Power required (W) Medium-size screen | Large-size screen | System cost |
|---|---|---|---|---|
| Electroluminscence | 0.4 | 2500 | No | High |
| Gas laser | 0.1 | 10 000 | 100 000 | High |
| Gas plasma | 0.25 | 4000 | No | Medium |
| CRT direct view | 4 | 250 | No | Medium |
| CRT projector | 0.5 | 2000 | 20 000 | High |
| Light valves | 4 | 250 | 2500 | Low |
| Solid-state lasers | 30 | 30 | 300 | Medium |

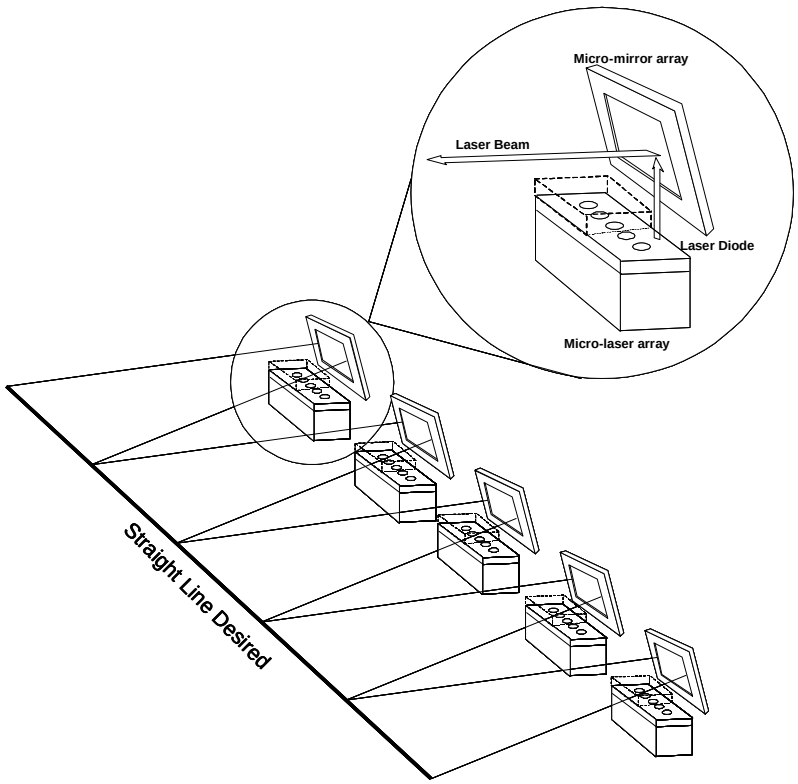


**Figure 4.** Printing mechanism of the micro-mirror and micro-laser arrays.

remaining part of the paper, the printer under study is assumed to have a resolution of 600 dpi with a nominal printing speed of 30 pages $min^{-1}$.

## 3. Analytical model of a cantilever beam

The proposed cantilever beam consists of a four-layer multimorph structure. A ZnO film is used as the piezoelectric layer and a p-doped polysilicon substrate is used both as the elastic layer and the bottom electrode. The elastic layer is needed to add structural damping in the system and to provide mechanical support for the thin ZnO film. The $Si_3N_4$ layer acts as the middle shim layer, providing an amorphous base layer for ZnO. It also provides a high residual tensile stress to offset the compressive stress in the ZnO film as well as preventing dc current leakage through the piezoelectric film. A thin layer of Pt sputtered on the structure, functions both as the top electrode and the reflective surface for the laser beam. In the following derivation, both the Pt and $Si_3N_4$ layers are neglected since their thicknesses are relatively small ($\sim$0.2 $\mu$m).

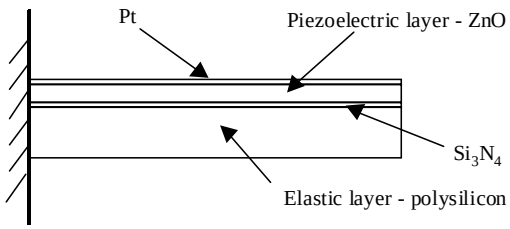


**Figure 5.** Structure of the cantilever beam.

When a piezoelectric element is stressed mechanically by a force or moment, an electrical charge is generated. When it is stressed electrically by an applied voltage, its dimensions change. This is the basic actuation principle of the device under study. The piezoelectric linear constitutive equations are given as

$$S_1 = s_{11}^E T_1 + d_{31} E_3 \tag{1}$$

$$D_3 = d_{31} T_1 + \varepsilon_{33}^T E_3 \tag{2}$$

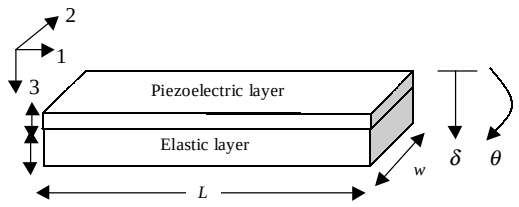


**Figure 6.** Physical dimensions of the cantilever beam.

where $S_1$ is the axial strain, $s_{11}^E$ is the mechanical compliance at constant electric field, $T_1$ is the axial stress, $d_{31}$ is the piezoelectric linear coupling coefficient and $E_3$ is the electric field applied across material in the 3-direction. $D_3$ is the electric displacement (charge per unit area) and $\varepsilon_{33}^T$ is the permittivity of the piezoelectric element at constant stress. The subscripts associated with the variables are directly related to the coordinate system used, as shown in figure 6. Equation (1) states that the mechanical strain in a piezoelectric material is proportional to both the applied stress (Hook's law) and the applied electric field (converse piezoelectric effect). Equation (2) states that the electric displacement is proportional to both the applied stress (direct piezoelectric effect) and the applied electric field (dielectric effect).

There are two basic approaches used to model the tip deflection and slope of a piezoelectric cantilever beam. Smits and Choi [16] used the internal energy approach to derive the constituent equations, relating the response parameters (tip deflection, tip rotation, volumetric displacement, electrode charge) to the driving parameters (tip force, tip moment, uniformly distributed force, electrical voltage). DeVoe [22] used a more familiar beam-theory-based derivation to derive the constituent equations that was originally developed by Timoshenko [23] in 1925 to model thermal bi-metallic strips. Both approaches applied the radius curvature equations for bending beams and yielded similar results. DeVoe simplified the equations by assuming a thin piezoelectric layer on a thick elastic substrate. The simplified equations with free boundary conditions (without external force or moment) are given as follows:

$$\delta = 3d_{31}\frac{L^2 E_p}{t_e^2 E_e}V \tag{3}$$

$$\theta = 6d_{31}\frac{L E_p}{t_e^2 E_e}V \tag{4}$$

where $\delta$ is the tip deflection, $\theta$ is the slope or tip rotation, $L$ is the length of the beam along the longitudinal axis, $t_e$ is the thickness of the elastic layer and $V$ is the external voltage applied across the electrodes, refer to figure 6. $E_p$ and $E_e$ is the Young's modulii of elasticity for the piezoelectric and elastic materials, respectively.

The tip motion of the bending beam can be separated into two distinct movements, a transverse deflection, $\delta$, and a rotational motion, $\theta$. Figure 7 illustrates the motion of tip of the beam. Due to the dimensions of the device and the nature of the application, both the full-scale deflection and the rotational angle are very small, in the orders of $10^{-7}$ inches and $10^{-4}$ radians respectively. Due to the geometrical scaling effects as can be seen in figure 7, the actual change of the beam position $Y$–$Y'$ is amplified only for the case of pure rotational motion. The full-scale laser beam position change

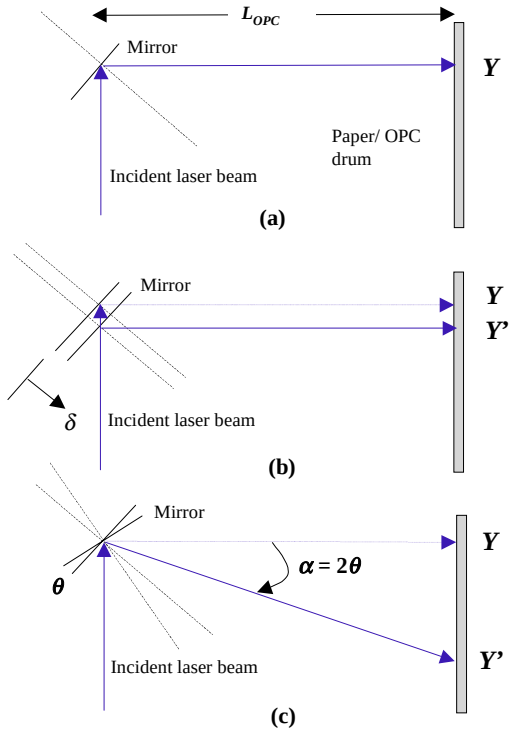


**Figure 7.** Motion of the tip mirror of the cantilever beam. (*a*) Laser beam position without any motion. (*b*) Laser beam position change with pure deflection, $\delta$. (*c*) Laser beam position change with pure rotation, $\theta$.

for the rotational case is in the order of $10^{-3}$ inches, which is approximately four orders larger than the effect of pure transverse deflection. Therefore, the effect of the transverse deflection can be safely neglected in the following derivations.

From the discussion above, it is clear that the value of the slope $\theta$ will determine the final laser beam position and the corresponding scan line spacing. More specifically, the relationship between the scan line spacing $\Delta Y$ and the slope at the tip of the beam is given by

$$\Delta Y = L_{OPC}\tan(2\theta). \tag{5}$$

Linearizing for small angles ($\theta \ll 1$), equation (5) can be simplified to

$$\Delta Y = L_{OPC}(2\theta) \tag{6}$$

where $L_{OPC}$ is the optical distance between the reflective point on the Pt layer and the paper/OPC drum. Therefore the value of the slope, $\theta$, is needed to characterize the behavior of the laser beam position $Y$. This motivated the approach of using rotational dynamics to model the piezoelectric cantilever beam as a lumped second-order system consisting of an equivalent rotational inertia, equivalent rotational stiffness and equivalent damping, as shown in figure 8.

### *3.1. Equivalent rotational stiffness*

From basic beam theory, the relationship between the tip deflection $\delta$ and slope $\theta$ of a cantilever beam and the applied point load $P$ and moment $M$ on the tip is given as

$$\delta = \left(\frac{L^3}{3EI}\right)P + \left(\frac{L^2}{2EI}\right)M \tag{7}$$

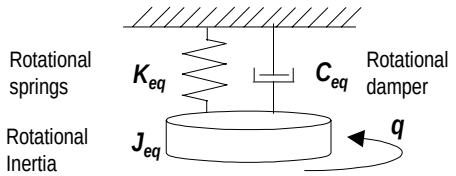


**Figure 8.** Equivalent lumped second-order model for the cantilever bending beam.

and

$$\theta = \left(\frac{L^2}{2EI}\right)P + \left(\frac{L}{EI}\right)M \tag{8}$$

where $E$ is the Young's modulus of elasticity of the beam, $I$ is the second moment of area about the bending axis, $L$ is the length of the beam and $A$ is the cross sectional area. The rotational stiffness of a cantilever beam is derived from equation (8) assuming only a pure moment acting on the tip of the beam. Therefore, the expression for the rotational stiffness is

$$K = \frac{EI}{L}. \tag{9}$$

Since the beam consists of two separate layers, equivalent rotational stiffness can then be expressed as

$$K_{eq} = \frac{E_p I_p}{L} + \frac{E_e I_e}{L} \tag{10}$$

where the subscripts $p$ and $e$ represent the piezoelectric and elastic materials, respectively.

### *3.2. Equivalent mass moment of inertia*

The equivalent mass moment of inertia was derived by transforming the continuous beam (distributed system) into a lumped discrete system consisting of a massless beam and an equivalent inertial load at the tip of the beam. This was done by equating the first natural frequency of a continuous cantilever beam with the natural frequency of a discrete lumped second-order model. From the Euler–Bernoulli beam theory, the $j$th natural frequency of a cantilever bending beam is given by [31]

$$\omega_j = (\beta L)_j^2 \left(\frac{EI}{\rho L^4 A}\right)^{1/2} \tag{11}$$

where $\rho$ is the density of the material and $\beta L$ is a unitless parameter that can be obtained by solving the following characteristic equation:

$$\cos(\beta L) = -\frac{1}{\cosh(\beta L)}.$$

For the first mode when $j$ equals one, $(\beta L)^2$ is calculated to be 3.5160. Using these results, the equivalent mass moment of inertia of the cantilever bending beam $J_{eq}$ was obtained by equating

$$\omega_n = \left(\frac{K}{J_{eq}}\right)^{1/2} = 3.5160\left(\frac{EI}{\rho L^4 A}\right)^{1/2}. \tag{12}$$

Substituting the expression for the rotational stiffness $K$ from equation (9) into equation (12), the expression for $J_{eq}$ was derived as follows:

$$J_{eq} = \frac{1}{3.560^2}(\rho AL)L^2 = 0.243\left(\frac{1}{3}\mathrm{m}_{beam}L^2\right) = 0.243J_{beam} \tag{13}$$

where $m_{beam}$ is the mass of the beam and $J_{beam}$ is the mass moment of inertia of the cantilever beam about the bending axis located at the base of the beam. The first natural frequency of the system $\omega_n$ was then derived using the equivalent rotational stiffness $K_{eq}$ and the equivalent mass moment of inertia $J_{eq}$ as

$$\omega_n = \left(\frac{K_{eq}}{J_{eq}}\right)^{1/2}. \tag{14}$$

### *3.3. Equivalent structural damping*

There are two different types of damping that occur during the operation of the piezoelectric beam deflection device. The first type is known as material damping, which is related to the energy dissipation in a material due to intermolecular forces and internal friction. The second type is called system damping, which involves the conversion between the electrical and mechanical energy of piezoelectric materials. The later is usually referred to as a nonlinear effect, better known as electromechanical hysteresis. Electromechanical hysteresis effects of the system will be neglected at this point since researchers commonly model electromechanical hysteresis separately from the structural damping of the system [18].

Damping arises from the removal of energy by thermal, acoustic or other types of radiation or dissipation. It is assumed here that material damping is the most significant damping component and damping effects due to interfacial contacts between the members are neglected. Material damping can be further categorized into viscous damping and structural damping. The viscous damping model is usually used for low-velocity, lubricated contacts. The viscous damping force is a linear continuous function of the velocity, which usually leads to a simpler set of mathematical equations. Structural damping is more complex in nature with nonlinear characteristics. The damping of structural material is often independent of the frequency of the system. Therefore, viscous-type damping is often not a realistic approximation of the damping characteristics of structural materials. However, for very small damping, structural damping can be approximated by a linear system with viscous-type damping. Numerous methods have been proposed in the literature to approximate structural damping using simplified models [26–31]. Structural damping is considered here as the main damping component for the piezoelectric cantilever beam.

Structural damping is generally measured and characterized under conditions of near-cyclic motion [26]. Therefore, a method to quantify the effects of damping is by comparing the energy loss in a cycle with the peak potential energy stored during the cycle. This quantity is known as the loss factor $\eta$, which is defined as

$$\eta = \frac{W_d}{2\pi U} \tag{15}$$

where $W_d$ is the energy loss per cycle and $U$ is the peak potential energy in the system. The loss factor for the device under study is assumed to be 30. The equivalent viscous damping was found by equating the energy dissipated by the

**Table 2.** Material and geometrical properties.

| Property | Symbol | Value | Unit |
|---|---|---|---|
| Piezoelectric material: ZnO | | | |
| Linear coupling | $d_{31}$ | $5 \times 10^{-12}$ | m V$^{-1}$ |
| Elasticity | $E_p$ | $161 \times 10^{9}$ | N m$^{-2}$ |
| Density | $\rho_p$ | 5660 | kg m$^{-3}$ |
| Loss factor | 0.30 | | |
| Dimensional properties | | | |
| Length | $L$ | $200 \times 10^{-6}$ | m |
| Thickness of ZnO film | $t_p$ | $0.5 \times 10^{-6}$ | m |
| Thickness of polysilicon film | $t_e$ | $8 \times 10^{-6}$ | m |
| Width | $w$ | $30 \times 10^{-6}$ | m |
| Other properties | | | |
| Mass of beam | $m_{beam}$ | $1.274 \times 10^{-10}$ | kg |
| Elastic modulus | $E_e$ | $150 \times 10^{9}$ | N m$^{-2}$ |
| Resistance of drive | $R_1$ | $6.75 \times 10^{3}$ | Ω |
| Capacitance of piezoelectric | $C_1$ | $4.90 \times 10^{-9}$ | F |
| Distance from beam tip to OPC | $L_{OPC}$ | 5.00 | inch |

viscous damping to that of the structural damping force with assumed harmonic motion. Assuming steady-state simple harmonic motion

$$\theta(t) = A\cos\omega t$$

and modeling the structural damping as an ideal linear damper $C_{eq}$, the damping force $F_d$ is given as

$$F_d = C_{eq}\frac{\mathrm{d}\theta}{\mathrm{d}t}.$$

The energy loss per cycle $W_d$ can then be expressed using

$$W_d = \int F_d\,\mathrm{d}\theta = \int_0^{2\pi/\omega} C_{eq}\left(\frac{\mathrm{d}\theta}{\mathrm{d}t}\right)^2 \mathrm{d}t = \pi C_{eq}\omega A^2. \quad (16)$$

The peak potential energy stored in the device during the cycle is equivalent to the peak energy stored in the effective rotational spring and is given as

$$U = \tfrac{1}{2}K_{eq}A^2. \quad (17)$$

Since the effect of damping is more significant near resonance, the loss factor is usually evaluated at the natural frequency, $\omega_n$. Substituting (16) and (17) into (15), the loss factor can be expressed as

$$\eta = \frac{C_{eq}\omega_n}{K_{eq}}. \quad (18)$$

Critical damping is another commonly used coefficient, given as

$$C_c = 2(K_{eq}J_{eq})^{1/2}. \quad (19)$$

Using the result from (18) and (19) and substituting the expression for the natural frequency $\omega_n$ given by (14), the equivalent damping ratio $\zeta$ is related to the loss factor $\eta$ as

$$\zeta = \frac{C_{eq}}{C_c} = \frac{1}{2}\eta. \quad (20)$$

Using equations (15)–(19), the equivalent damping ratio was calculated to be 0.15, which corresponds to 15% structural damping in the system.

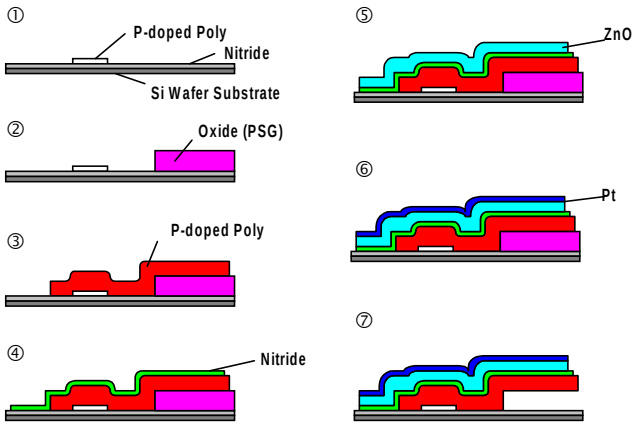


**Figure 9.** Proposed fabrication process of the cantilever beam for micro-mirrors.

### *3.4. Lumped dynamical model*

Using the derived equations for the equivalent rotational inertia, rotational stiffness and damping, a lumped second-order dynamic model for the cantilever beam deflection device was obtained. The transfer function relating the slope $\theta(s)$ to the applied moment $M(s)$ is given as

$$G(s) = \frac{\theta(s)}{M(s)} = \frac{1}{J_{eq}s^2 + C_{eq}s + K_{eq}}. \quad (21)$$

Using the system static gain obtained from (4), the relationship between the slope $\theta(s)$ and the applied voltage $V(s)$ can be expressed as

$$\frac{\theta(s)}{V(s)} = 6d_{31}\frac{LE_p}{t_e^2E_e}\frac{K_{eq}}{J_{eq}s^2 + C_{eq}s + K_{eq}}. \quad (22)$$

However, only part of the electrical energy supplied to the piezoelectric beam is converted into mechanical strain. The piezoelectric beam is also a capacitor capable of storing electrical energy because of its electromechanical coupling properties. The system is more accurately modeled by including a first-order resistance–capacitance ($RC$) circuit preceding the second-order cantilever bending beam model.

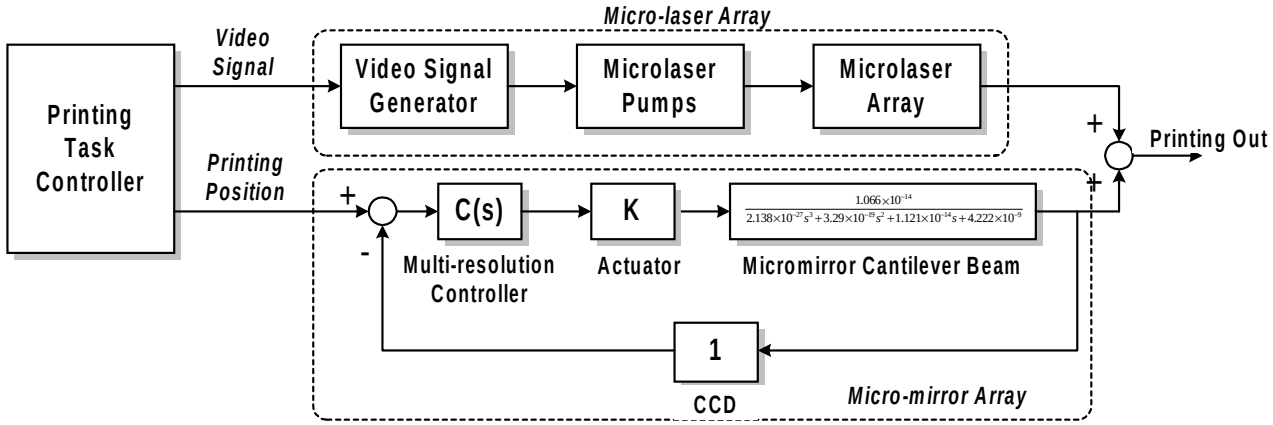


**Figure 10.** Block diagram of the overall control system.

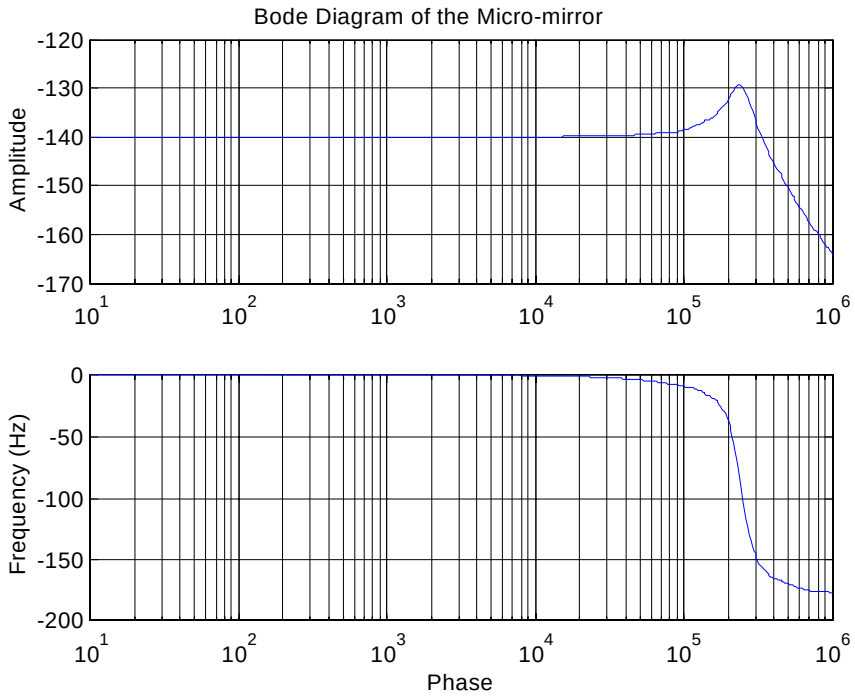


**Figure 11.** Frequency response of the micro-mirror system.

The transfer function representing the $RC$ circuit is given as

$$L(s) = \frac{1}{R_1 C_1 s + 1} = \frac{1}{3.307 \times 10^{-5} + 1} \tag{23}$$

where $R_1$ is the total impedance of the drive circuit and $C_1$ represents the dielectric properties of the piezoelectric material with the typical values for $R_1$ and $C_1$ given in table 2. Using the models obtained from (22) and (23) as well as the scaling laws derived in (6), the micro-mirror device is modeled as a third-order system of the form

$$\frac{Y(s)}{V(s)} = 2L_{OPC} \times \frac{1}{R_1 C_1 s + 1} \times 6d_{31} \frac{LE_p}{t_e^2 E_e} \frac{K_{eq}}{J_{eq} s^2 + C_{eq} s + K_{eq}} \quad [\text{inch V}^{-1}] \tag{24}$$

relating the output scan line position $Y(s)$ to the applied electrical voltage $V(s)$. Substituting the values from table 2 into (24) yields

$$\frac{Y(s)}{V(s)} = [9.663 \times 10^{-10}][2.683 \times 10^{-27} s^3 + 4.139 \times 10^{-19} s^2 + 1.951 \times 10^{-13} s + 9.603 \times 10^{-7}]^{-1}. \tag{25}$$

Using the model derived for a print resolution of 600 dpi, a one-pixel deflection can be achieved with a 2 V voltage swing. This movement is adequate to compensate for banding since the line placement errors are usually within 50% of the nominal line spacing.

## 4. Proposed fabrication process

The cantilever micro-mirrors can be fabricated using the following proposed procedures, as also illustrated in figure 9. Such processes have been described extensively in literature in the past [34, 35]. The process flow starts with a ⟨100⟩ silicon wafer with a thin silicon nitride passivation layer. A

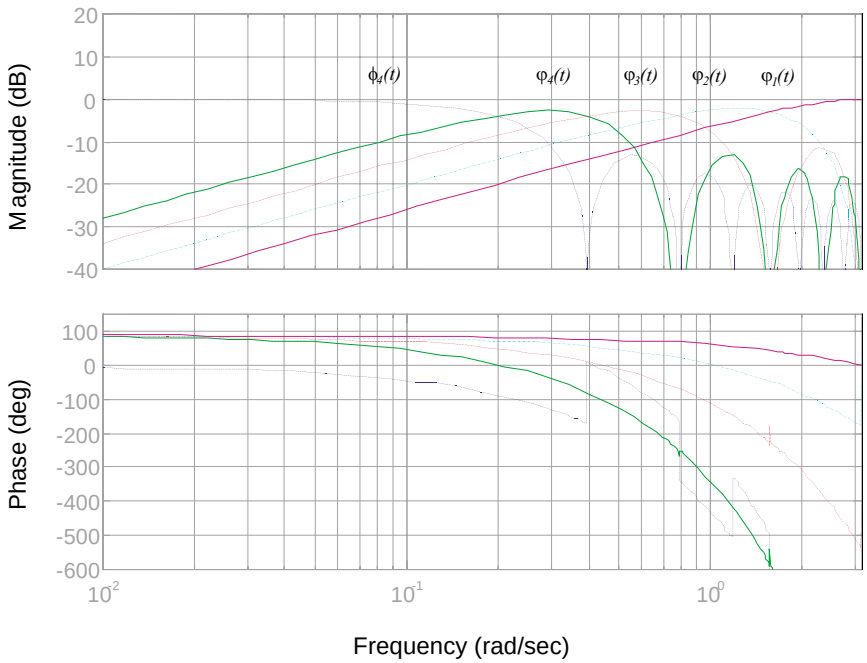


**Figure 12.** Frequency response of the micro-mirror system.

ground layer of LPCVD phosphorous-doped polysilicon is then deposited as the bottom electrode contact. Next, a layer of PSG (phosphosilicate glass, 2 $\mu$m) was deposited followed by reactive ion etching (RIE) to form a cantilever mesa. Then the p-doped polysilicon is deposited to form primary elastic layer of the cantilever structure. After that, $Si_3N_4$ is deposited to isolate the polysilicon layer and the piezoelectric layer. ZnO is then deposited via RF sputtering followed by thermal annealing at $T = 500\,^{\circ}$C to reduce the highly compressive residual stress of the ZnO layer. Pt is then sputtered on the structure as the top electrode. Finally the structures can be released using a photoresist mask in buffered hydrofluoric acid followed by $CO_2$ supercritical drying to form the cantilever structure.

## 5. Controlled design

The controller designed for the proposed printing system can be divided into two major parts. The first part is the digital signal converter to convert the video signal into discrete pulses of the micro-laser array. The second part is a closed-loop controller to compensate for image banding caused by the mechanical disturbances. Figure 10 shows the block diagram of the overall control system.

### *5.1. Data conversion*

To print the digital image properly, the bandwidth of the micro-laser array must be sufficient to convert the image signal into discrete pulses. Since the print resolution is 600 dpi and the printing speed is 30 pages min$^{-1}$, the switching frequency is calculated to be 3.6 kHz using the following equation:

$$600 \text{ dpi} \times 12 \text{ inches} \times 30 \text{ pages min}^{-1} = 3.6 \text{ kHz} \qquad (26)$$

where 12 inches represents the total length of a paper in the process direction. The bandwidth of a typical micro-laser diode is usually more than 1 MHz. Therefore, the digital data converter has enough bandwidth to convert the data.

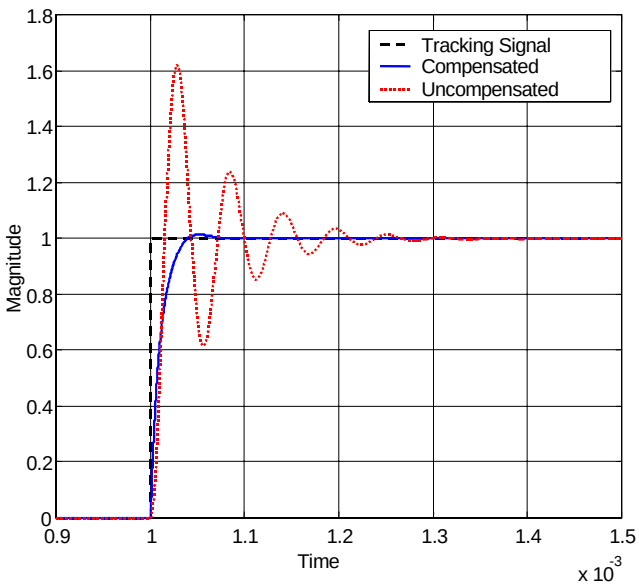


**Figure 13.** Step response of the micro-mirror system.

### *5.2. Closed-loop control*

To reduce banding, the system needs a well defined tracking controller. To avoid aliasing, the bandwidth of micro-mirror needs to be at least twice that of the micro-laser bandwidth. Based on Shannon's sampling theorem, a bandwidth of 7.2 kHz will be needed for the system under study. From the frequency response of the system in figure 11, the bandwidth of the micro-mirror device is more than 200 kHz. The lightly damped resonant peak at 250 kHz will cause excessive ringing and could lead to premature failure of the structure due to cyclic stresses. Therefore, it is the control objective to attenuate the oscillations as fast as possible. Using the model given in (25), a feedback control strategy is proposed to track the line spacing errors accurately and eliminate image banding.

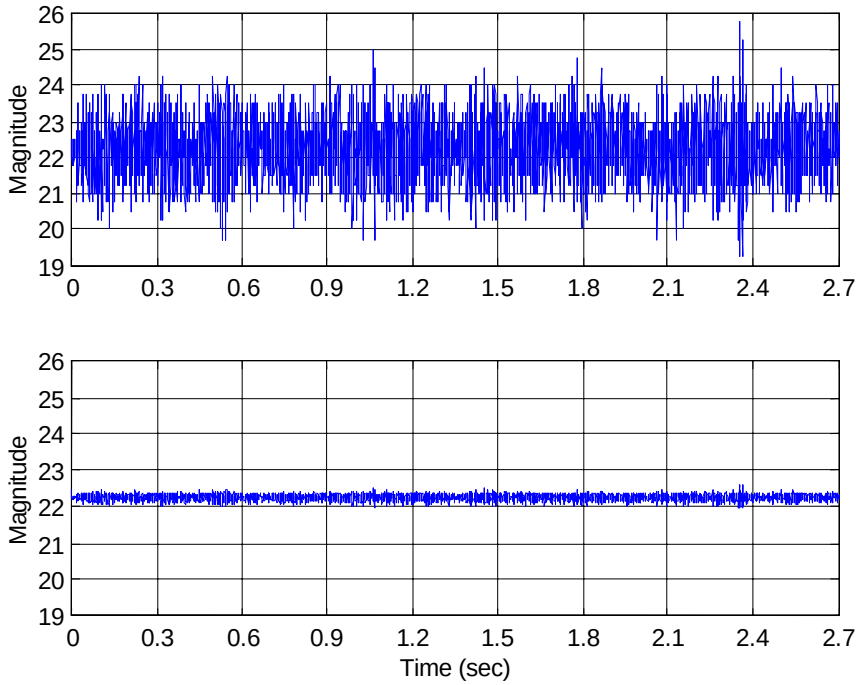


**Figure 14.** Line spacing time history of the printout signal before and after compensation.

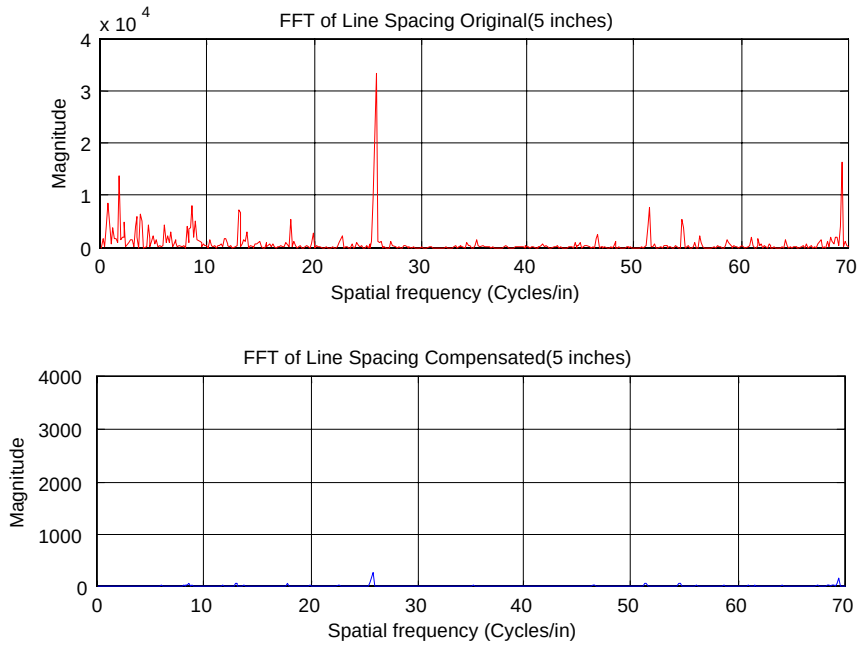


**Figure 15.** Power spectrum of line spacing before and after compensation.

Figure 10 shows the block diagram of the closed-loop control system. A CCD element will be used as a sensor to detect the scan line variation on the OPC drum.

A new type of nonlinear controller using multi-resolution theory will be applied to achieve the control objective. The multi-resolution control theory decouples the original system into several sub-systems in different frequency bands, and each band contains a separate frequency range. By applying the control algorithm, the properties at each frequency range can be derived separately. By loop shaping the various frequency bands, the controller is designed as the combination of several parallel lead-lag controllers. The Bode diagram of the original model is shown in figure 11, and the Bode diagram of the wavelet transform mapping is shown in figure 12.

Based on the wavelet algorithm, the multi-resolution controller was decoupled into different frequency bands by stretching the wavelet function. The Haar wavelet transform could be expressed as

$$a_n(t) = \sum_{k=0}^{2^{n-1}-1} a_{n-1}(t-k)\cdot\phi_n(k) = a_{n-1}(t-k)\otimes\phi_n(k) \quad (27)$$

$$d_n(t) = \sum_{k=0}^{2^{n-1}-1} a_{n-1}(t-k)\cdot\varphi_n(k) = a_{n-1}(t-k)\otimes\varphi_n(k) \quad (28)$$

where $a_n(t)$ and $d_n(t)$ is the $n$th-level wavelet coefficient, $\varphi_n(t)$ is the $n$th-level wavelet function and $\phi_n(t)$ is the $n$th-level scaling function. By applying a $Z$-transform, the transfer function of the multi-resolution controller can then be described as

$$A_k(z) = \left(\frac{1}{2}\right)^k \prod_{n=1}^{k} \frac{z^n + 1}{z^n}$$

$$D_k(z) = \left(\frac{1}{2}\right)^k \frac{z^k + 1}{z^k} \prod_{n=1}^{k-1} \frac{z^n + 1}{z^n} \tag{29}$$

and the transfer function of the controller is

$$C_n(z) = a_k \cdot A_k(z) \oplus d_K \cdot D_k(z) \oplus d_{k-1} \cdot D_{k-1}(z) \oplus \cdots \oplus d_1 \cdot D_1(z) \tag{30}$$

where $a_k$ and $d_k$ are the control coefficients of the $k$th level and $A_k(z)$ and $D_k(z)$ are the transfer functions of each level. By compensating the system in each level, the controller could eliminate all the peaks in each frequency band and achieve the desired zero steady-state error criteria in a finite duration. This satisfies both the tracking objective and the desired transient response (reduced oscillations).

## 6. Simulation and emulation results

Figure 13 shows the simulation result of a unit step response. The oscillations of the original system are compensated for and the output converges quickly. The 60% overshoot of the system is reduced to less than 2% with the feedback controller. By using an actual sequence of measured line spacing data from an experimental laser printer, the operation of the system using the micro-mirror array to compensate for banding was simulated. Using a 5 inch long sequence, three performance measures were used to evaluate the effectiveness of the micro-mirror device in reducing banding. The actual line spacing variation before and after control can be seen in figure 14. The magnitude of the line spacing variation or the error band was significantly reduced using the micro-mirror arrays to compensate for the line positioning errors. Figure 15 shows the power spectrum of the line spacing. It can be seen that the peaks at the lower frequencies are dramatically reduced, indicating better performance. Researchers have shown that low-frequency components ($<$50 cycles/inch) are more visible to the human eye [32]. Therefore, eliminating the periodic components in the lower frequency range should be sufficient to reduce the perception of banding.

To emulate the printout of the laser printer, the disturbance signal was applied to an actual grayscale image. The emulated printouts for both the uncompensated and compensated images are shown in figure 16. As shown by the power spectrum of the line spacing, the micro-mirror deflection device significantly reduced the appearance of banding in the printouts, demonstrating the effectiveness of this method.

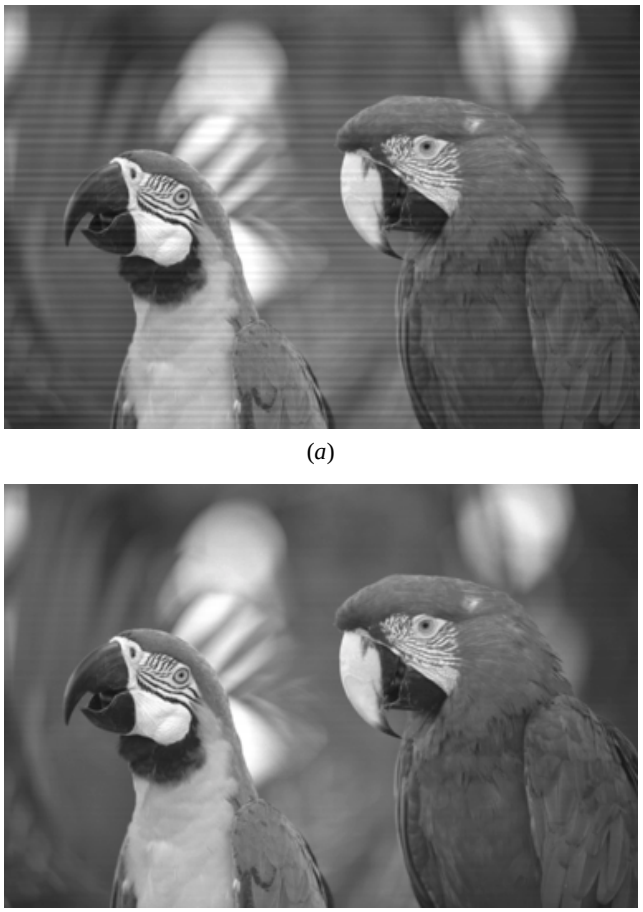

(*a*)

(*b*)

**Figure 16.** Emulated printout (*a*) before compensation and (*b*) after compensation.

## 7. Conclusions

The analytical model for the thin-film ZnO cantilever beam of a micro-mirror device was derived in detail. Using the dynamical model, a closed-loop control strategy was employed to improve the transient response and improve tracking performance to reduce image banding in the EP process. Simulated results showed a significant reduction of the errors at the main banding frequencies. The emulated images demonstrate the effectiveness of this method in reducing the image artifacts in digital EP printers. Micro-technology is an excellent choice of solution for this application because of the required micro-positioning accuracy and precision. As the dimension of the cantilever beam is scaled down the mechanical resonance of the beam is pushed to higher frequencies, thus increasing the bandwidth of the overall system. The added bandwidth can be exploited to achieve higher printing speeds and possibly higher printing resolution. Since MEMS devices can be batch fabricated, the overall production cost can also be significantly reduced, making this method an attractive solution in the near future.

## Acknowledgment

The authors would like to thank Hewlett Packard for their partial support of this work and for reviewing this paper.

## References

[1] Loce R, Lama W and Maltz M 1995 Modeling vibration-induced halftone banding in a Xerographic laser printer *J. Electron. Imag.* **4** 48–61

[2] Schubert P 1986 Periodic image artifacts from continuous-tone laser scanners *Appl. Opt.* **25** 3880–4
[3] Burns P, Rabbani M and Ray L 1986 Analysis of image noise due to position errors *Appl. Opt.* **25** 2158–68
[4] Kawamoto H, Udagawa K and Mori M 1995 Vibration and noise induced by electrostatic force on a contact charger roller of electrophotography *J. Imag. Sci. Technol.* **39** 477–80
[5] Kawamoto H 1995 Chatter vibration of a cleaner blade in electrophotography *Proc. IS&T's 11th Int. Congress on Advances in Non-Impact Printing Technologies* p 238
[6] Melnychuck P and Shaw R 1988 Fourier spectra of digital halftone images containing dot-position errors *J. Opt. Soc. Am.* **5** 1328–38
[7] Loce R, Lama W and Nylen P 1991 Multi-beam scanning system compensated for banding *US Patent Specification* 4989019
[8] Foote W and Servier R 1998 Laser printer with apparatus to reduce banding by servo adjustment of a scanned laser beam *US Patent Specification* 5760817
[9] Lawton R and Marshall D 1999 Beam deflecting for resolution enhancement and banding reduction in a laser printer *US Patent Specification* 5920336
[10] Kiang M H, Solgaard O, Muller R S and Lau K Y 1996 Surface-micromachined electrostatic-comb driven scanning micromirrors for barcode scanners *Proc. IEEE MEMS* pp 192–7
[11] Toshiyoshi H and Fujita H 1996 Electrostatic micro torsion mirrors for an optical switch matrix *J. Microelectromech. Syst.* **5** 231–7
[12] Sugihwo F, Larson M C and Harris J S Jr 1998 Micromachined widely tunable vertical cavity laser diodes *J. Microelectromech. Syst.* **7** 48–55
[13] Zou J, Balberg M, Byrne C and Liu C 1999 Optical properties of surface micromachined mirrors with etch holes *J. Microelectromech. Syst.* **8** 506–13
[14] Ernstoff M N, Valley G C and Shields S E 1999 Full color sequential image projection system incorporating time modulated illumination *US Patent Specification* 5903323
[15] Hargis D E, Flint G and Assa S 1999 High resolution image projection system and method employing lasers *US Patent Specification* 5990983
[16] Smits J G and Choi W S 1991 The constituent equations of piezoelectric heterogeneous bimorphs *IEEE Trans. Ultrasonics, Ferroelectrics Frequency Control* **38** 256–70
[17] Smits J G and Ballato A 1994 Dynamic admittance matrix of piezoelectric cantilever bimorphs *J. Microelectromech. Syst.* **3** 105–11
[18] Low T S and Guo W 1995 Modeling of a three-layer piezoelectric bimorph beam with hysteresis *J. Microelectromech. Syst.* **4** 230–7
[19] Smits J G, Choi W S and Ballato A 1997 Resonance and antiresonance of symmetric and asymmetric cantilevered piezoelectric flexors *IEEE Trans. Ultrasonics, Ferroelectrics, Frequency Control* **44** 250–7
[20] Blanguernon A, Lene F and Bernadou M 1999 Active control of a beam using a piezoceramic element *Smart Mater. Struct.* **8** 116–24
[21] Chen B M, Lee T H, Hang C C, Guo Y and Weerasooriya S 1999 An $H_\infty$ almost disturbance decoupling robust controller design for a piezoelectric bimorph actuator with hysteresis *IEEE Trans. Control Syst. Technol.* **7** 160–73
[22] DeVoe D 1997 Thin film zinc oxide microsensors and microactuators *PhD Dissertation* School of Mechanical Engineering, University of California, Berkeley
[23] Timoshenko S 1925 Analysis of bi-metal thermostats *J. Opt. Soc. Am. Rev. Sci. Instrum.* **11** 233–56
[24] IEEE 1987 *IEEE Standard on Piezoelectricity* ANSI/IEEE Std. 176-1987
[25] Moseley P and Crocker A 1996 *Sensor Materials* (Bristol: Institute of Physics)
[26] Crandall S H 1970 The role of damping in vibration theory *J. Sound Vib.* **11** 3–18
[27] Lazan B J 1959 Energy dissipation mechanisms in structures with particular reference to material damping *ASME Struct. Damp.* 1–34
[28] Tse F S, Morse I E and Hinkle R T 1978 *Mechanical Vibrations: Theory and Applications* (Boston, MA: Allyn and Bacon)
[29] Rao S S 1990 *Mechanical Vibrations* (New York: Addison-Wesley)
[30] Beards C F 1996 *Structural Vibration: Analysis and Damping* (New York: Arnold)
[31] Thomson W and Dahleh M 1998 *Theory of Vibrations with Applications* (Englewood Cliifs, NJ: Prentice-Hall)
[32] Nasanen R 1984 Visibility of halftone dot textures *IEEE Trans. Syst. Management Cybernetics* **14** 920–4
[33] Mallat S 1999 *A Wavelet Tour of Signal Processing* (Cambridge: Academic)
[34] DeVoe D L and Pisano A P 1997 Modeling and optimal design of piezoelectric cantilever microactuators *J. Microelectromech. Syst.* **6** 266–70
[35] Lee S S and White R M 1998 Piezoelectric cantilever acoustic transducer *J. Micromech. Microeng.* **8** 230–8

**Annotations from 22920ae.pdf**

**Page 3**

*Annotation 1*
`Hargis et al [15]' OK as set to match references?

*Annotation 2*
`rare earth' as intended?

**Page 4**

*Annotation 1*
Should figure 5 be cited in this paragraph?

*Annotation 2*
Definition of `CRT' OK? `Power required' in watts OK? Caption OK as set?

**Page 7**

*Annotation 1*
Definition of `RC' OK?

*Annotation 2*
Please clarify length and width of what in table 2?

*Annotation 3*
`inch' OK as set to match text?

**Page 8**

*Annotation 1*
`table 2' as intended?

*Annotation 2*
Units OK in (24)?

**Page 9**

*Annotation 1*
Please define `LPCVD'

*Annotation 2*
Definitions of `RIE' and `BHF' OK?

*Annotation 3*
Equation (26) OK to keep numbering the same?

**Page 12**

*Annotation 1*
Are [24] and [25] cited? Also, is [24] OK as set?

*Annotation 2*
Please supply volume number for [27]

*Annotation 3*
Are [33] to [35] cited? Also, is Cambridge (UK) OK in [33] or `Cambridge, MA'?